Journal of Catalysis 438 (2024) 115724

Contents lists available at ScienceDirect

Journal of Catalysis

journal homepage: www.elsevier.com/locate/jcat

Theoretical investigation of CO oxidation over polyoxometalate-supported Au cluster catalyst

Tomohisa Yonemori [a], Yasutaka Hamada [a], Tamao Ishida [b], Toru Murayama [c], Takashi Kawakami [a], Shusuke Yamanaka [a], Mitsutaka Okumura [a,d,*]

[a] Department of Chemistry, Graduate School of Science, Osaka University, Toyonaka, Osaka 563-0043, Japan
[b] Department of Applied Chemistry for Environment, Graduate School of Urban Environmental Sciences, Tokyo Metropolitan University, 1-1 Minami-osawa, Hachioji, Tokyo 192-0397, Japan
[c] Institute for Catalysis, Hokkaido University, Sapporo, Hokkaido 001-0021, Japan
[d] Innovative Catalysis Science Division, Institute for Open and Transdisciplinary Research Initiatives (ICS-OTRI), Osaka University, 1-1 Yamada, Suita, Osaka 565-0871, Japan

ARTICLE INFO

Keywords:
Au cluster catalyst
Au/POM
CO oxidation
DFT

ABSTRACT

A polyoxometalate-supported Au cluster catalyst (Au/POM) exhibited high catalytic activity for CO oxidation at room temperature; however, its activity decreased at the reaction temperature above 60 ℃. Density functional theory calculations were performed to elucidate the unique catalytic activities. Our calculations show that the interactions between water molecules accommodated within the defect site of the support and the O_2 adsorbed on the Au cluster generate active OOH^- species. This OOH^- species reacts readily with CO, resulting in high CO oxidation catalytic activity between −40 and 40 degrees Celsius. The activation barrier of CO oxidation over Au/POM in the presence of H_2O is much lower than that in the absence of H_2O. This is in good agreement with the experimental results, indicating that surface-adsorbed water allows for high CO oxidation catalytic activity around room temperature, whereas the activity decreases at higher temperatures owing to the desorption of surface-adsorbed water molecules.

1. Introduction

Au clusters supported on selected metal oxides exhibit high catalytic activity for low-temperature CO oxidation [1–3], the water–gas shift reaction [4,5], selective oxidation of propylene [6,7], aerobic oxidation of alcohols [8], etc., [9] while bulk gold is chemically inert. Numerous studies have been conducted to elucidate the nature of Au-cluster catalysts, particularly the mechanism of CO oxidation [10]. Because CO oxidation over Au cluster catalysts is highly active below 0 °C [1], the purification of polluted air using these catalysts has been attracting much attention. As a result of tremendous effort, the reaction mechanism of CO oxidation over Au cluster catalysts have been uncovered in recent years [3,9,10–13].

In the case of Au/rutile-TiO_2, many experimental and theoretical studies have investigated the nature of active oxygen, the effect of moisture, and the effect of lattice oxygen vacancy [11–24]. In the first step of the reaction, the O_2 adsorbed on the pentacoordinated Ti sites on the rutile-TiO_2 surface is activated by accepting electrons from Au/TiO_2. The donated electrons occupy the antibonding π* orbitals of O_2, weakening its bond and producing active oxygen species. Thus, the reaction between CO and O_2, and the dissociation of the O–O bond to form gaseous CO_2, are facilitated by the formation of active oxygen species [17,18]. Additionally, the perimeter of the Au cluster is important for CO activation; therefore, the dual-perimeter sites, including the perimeter of the Au cluster and the pentacoordinate Ti sites adjacent to the cluster, are thought to be the active sites for this reaction [19,20]. Some studies have also suggested that the existence of an oxygen vacancy site at the surface of the metal oxide support facilitates CO oxidation because the activation ability of O_2 on the reduced surface is stronger than that on the stoichiometric surface [21–23]. In addition, the formation of oxygen vacancies is the first step in the Mars–van Krevelen-like CO oxidation mechanism proposed by Behm et al [25]. A notable feature of

Abbreviations: DFT, density functional theory; VASP, Vienna ab initio simulation package; VESTA, Visualization for Electronic and Structural Analysis; POM, polyoxometalate.

* Corresponding author at: Department of Chemistry, Graduate School of Science, Osaka University, Toyonaka, Osaka 563-0043, Japan.
E-mail address: ok@chem.sci.osaka-u.ac.jp (M. Okumura).

https://doi.org/10.1016/j.jcat.2024.115724
Received 13 June 2024; Received in revised form 18 August 2024; Accepted 21 August 2024
Available online 22 August 2024

Au cluster catalysts is that their CO oxidation activity at low temperature is enhanced by the addition of water to the reaction gas [12,14–16]. Water molecules adsorbed on the surface enable active OOH species, which readily react with CO by donating a proton to the adsorbed O_2 [15]. Therefore, Au cluster catalysts can facilitate low-temperature CO oxidation in the presence of water molecules on not only reducible metal oxides but also non-reducible oxides, such as SiO_2 and Al_2O_3, which cannot directly activate adsorbed O_2 [12].

The immobilization of Au clusters on various materials and metal oxides is important for the further development of Au cluster catalysts. Au clusters of <2 nm supported on alkaline earth metal hydroxides such as $Mg(OH)_2$ and $Be(OH)_2$ exhibit high CO oxidation activity—even at –73 °C [26–30]. However, Au/$Mg(OH)_2$ is readily deactivated by the formation of carbonate species, which block the active sites [27]. Lian et al. reported that Au clusters supported on metal carbonates such as $CaCO_3$ and $BaCO_3$ exhibit high CO oxidation activity when the reaction gas contains a certain amount of water [31]. Phonthammachai et al. immobilized Au clusters on hydroxyapatite (HAP), but only in the high-temperature region (100–150 ℃) did this catalyst show CO oxidation activity [32]. This is thought to be because the heterojunction between the Au clusters and HAP is worse at activating O_2 than conventional metal oxide-supported Au cluster catalysts.

Polyoxometalate (POM), a porous ionic crystal composed of a metal oxide anion cluster and its countercationic moiety, has been used in many fields such as green catalysis, medicine, surface science, and material science, among others [33–35]. Despite much attention being paid to the usability of POM, only a few studies have used POM as a support for metal cluster catalysts. Yoshida et al. reported that an Au cluster with a 2.0 nm diameter supported on Keggin-type silicotungstate polyoxometalate salt $Cs_4[SiW_{12}O_{40}]$ exhibits high CO oxidation activity, with almost 100 % conversion below 0 °C [36]. In contrast to its high catalytic activity at low temperatures, its activity decreased at the reaction temperature above 60 °C. Such an inverted, U-shaped catalytic activity with respect to the reaction temperature was also observed for Au/$Mg(OH)_2$ owing to the formation of carbonate species, which block the active perimeter interface [28]. However, for Au/POM, no deactivation of the CO oxidation reaction was observed, even after 35 days. Thus, the activity decrease at high temperatures was not due to catalyst deactivation. An investigation of the relationship among CO conversion, water vapor pressure during the reaction, and reaction time indicates that the water molecules remaining on the surface play an important role in the catalytic reaction. DRIFT measurements revealed a decrease in the amount of water molecules adsorbed on the catalyst above 60 ℃, which is thought to be related to the decrease in catalytic activity in the high-temperature region [36]. However, the details of this catalytic reaction have not been completely elucidated.

In the present study, we focused on the role of water molecules in O_2 activation. Specifically, we investigated the mechanisms of CO oxidation over Au/POM with and without water molecules using DFT calculations. From these calculations, we determined that water molecules play a critical role in O_2 activation and enable the catalyst to undergo CO oxidation at low temperatures. This is the first theoretical study shedding light on the effect of water addition on the activity of Au/POM catalysts for CO oxidation by changing the reactive oxygen species produced during catalytic reactions.

2. Computational details

Density functional theory (DFT) calculations with periodic boundary conditions were performed using the Vienna Ab initio Simulation Package (VASP 5.4) [37,38]. GGA-PBE [39] was used as the exchange–correlation functional, and the projector-augmented wave function method (PAW) [40,41] was used to calculate the potentials of the core electrons. The PAW potentials of the H(1 s^1), C($2s^2 2p^2$), O($2s^2 2p^4$), Si($3s^2 3p^2$), Cs($5s^2 5p^6 6s^1$), W($5d^4 6s^2$), and Au($5d^{10} 6s^1$) valence electron configurations were adopted. The differential charge of each atom was calculated by subtracting the number of electrons from the Bader charge [42]. The plane-wave basis set was adopted as the basis function, where 400 eV was the cutoff energy of the plane-wave expansion, and a Monkhorst–Pack k-point mesh [43] of 1 × 2 × 1 was used to integrate the reciprocal space. For W atoms, U – J=3.0 eV allowed correct calculation of the strongly correlated compounds [44]. The total energy self-consistency criterion was set to 1 × 10^{-6} eV. The dispersion effect was also considered in all calculations by using the DFT+D3 approach [45].

The structures of the equilibrium (EQ) state and transition state (TS) were relaxed until the maximum force was smaller than 0.01 eV \AA^{-1}. To relax each structure, the conjugate gradient algorithm [46,47] and quasi-Newton algorithm [48,49] were used for the EQ and TS, respectively. To locate the TS, the VTST tool was used with the climbing nudged elastic band (cNEB) [50–54] and dimer [55–58] methods. Constraint optimization with a fixed bond length of two atoms was also used to locate the TS in an atomic simulation environment (ASE) [59]. Vibrational analysis verified that all the TS structures had only one imaginary frequency. VESTA [60] was used to visualize the structures.

As shown in Fig. 1(a), the structure of $[SiW_{12}O_{40}]^{4-}$ corresponds to a Keggin-type POM. The crystal structure of $Cs_4[SiW_{12}O_{40}]$ was based on those reported in previous studies [61–65] and is known to have one $[SiW_{12}O_{40}]^{4-}$ defect site (out of four) to compensate for the excess negative charge of $[SiW_{12}O_{40}]^{4-}$. Therefore, $Cs_4[SiW_{12}O_{40}]$ is a porous material with 0.6 nm pores, as shown in Fig. 1(b) [64]. The size of the Au clusters in the previous study (2.0 nm) was larger than that of the pores (0.6 nm) of $Cs_4[SiW_{12}O_{40}]$ [36], indicating that the Au clusters cannot be anchored in the pores. Water molecules can fill defect sites under wet conditions [65]. Based on these results, Au-supported model structures were constructed; those with Au_{10} clusters anchored to the surface of $Cs_4[SiW_{12}O_{40}]$ are shown in Fig. 1(c) and (d). The structures contain three $[SiW_{12}O_{40}]^{4-}$ anions, twelve Cs atoms, and an Au_{10} cluster. As shown in Fig. 1(d), six water molecules were introduced into the anion vacancies of the model structure shown in Fig. 1(c). The structures of the water molecules are shown in Fig. 1(e). The number of water molecules in the defect site of POM in the slab model in Fig. 1(d) is the minimum number where Cs^+ does not migrate significantly toward the defect site. During the optimization of the structure, atoms included above the top layer (Au_{10}, $[SiW_{12}O_{40}]^{4-}$ (1), $5Cs^+$, and H_2O molecules) were only relaxed, and the atoms in the bottom layer were fixed. The adsorption energies for Au_{10}, O_2, and CO were calculated using the following equation:

$$E_{ads}(A) = E(A/M) - E(M) - E(A) \quad (1)$$

where $E_{ads}(A)$ is the adsorption energy of adsorbate A on surface model M, and E(x) is the total energy of x. The adsorption energies of Au_{10} ($E_{ads}(Au_{10})$) are –1.43 eV and –1.39 eV on the models with and without six water molecules, respectively. The size of the lattice of this slab model is 23.1 × 11.5 × 31.5 \AA, and it contains a 17.8 \AA vacuum region above the surface of the catalyst. The x, y, and z coordinates of Au_{10}/POM with six water molecules shown in Fig. 1(d) are summarized in Table S1.

3. Results and discussion

3.1. Heterojunction effect between Au_{10} and POM

It is well known that the active site for CO oxidation over Au cluster catalysts is the interface between the Au cluster and support [9]. Thus, we investigated the heterojunction effect between Au_{10} and POM based on the differential charge density of Au_{10}/POM using a slab model with water molecules. The results are shown in Fig. 2. The differential charge density, Δρ, was calculated using Eq. (2):

$$\Delta\rho = \rho_{Au/POM} - \rho_{Au} - \rho_{POM} \quad (2)$$

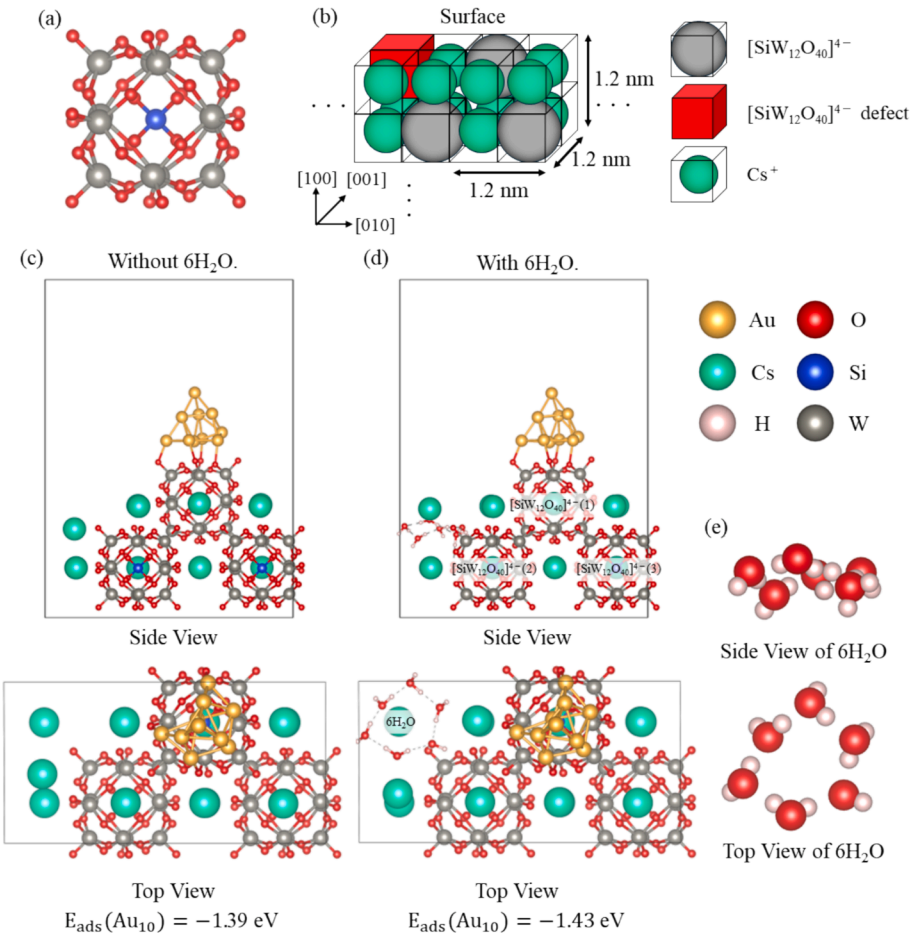

Fig. 1. Structures related to $Au/Cs_4[SiW_{12}O_{40}]$. (a) Structure of anionic Keggin-type POM $[XM_{12}O_{40}]^{n-}$. The blue ball inside the core structure is heteroatom X (e.g., P, Si, or As), the gray balls outside the core structure are metal atoms M (e.g., W, Mo, and V), and the red balls outside the core structure are O atoms. (b) Structure of $Cs_4[SiW_{12}O_{40}]$ with a defect site. (c) Side and top views of the slab model of Au_{10}/POM without water molecules. (d) Side and top views of the slab model of Au_{10}/POM with six water molecules in its defect site. (e) Side and top views of $6H_2O$ in the defect site of $[SiW_{12}O_{40}]^{4-}$ in the slab model. (For interpretation of the references to colour in this figure legend, the reader is referred to the web version of this article.)

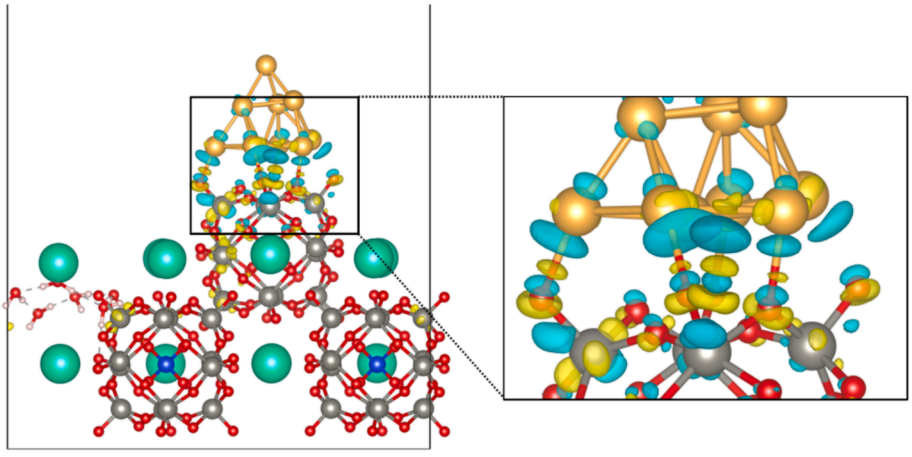

Fig. 2. Differential charge density $\Delta\rho$ of Au_{10} immobilized on $Cs_4[SiW_{12}O_{40}]$. The yellow/blue zones represent electron accumulation/depletion areas induced by Au_{10} immobilization. The isosurface was set to 0.001 e/\AA. (For interpretation of the references to colour in this figure legend, the reader is referred to the web version of this article.)

where $\rho_{Au/POM}$, ρ_{Au}, and ρ_{POM} are the charge densities of Au_{10}/POM, Au_{10}, and POM, respectively. Here, ρ_{Au} and ρ_{POM} were calculated using structures identical to those of Au_{10}/POM. It can be seen that the electron-accumulated areas (yellow) are located on the $[SiW_{12}O_{40}]^{4-}$ site of the interface between Au_{10} and POM, and the electron-depleted areas (blue) appear around Au_{10}. The results of the Bader charge analysis for each component of the models are listed in Table 1. The total negative charge of each $[SiW_{12}O_{40}]^{4-}$ increased, and Au_{10} had a positive

Table 1
Differential charges of each component in the models investigated. POM, Au_{10}/POM, and O_2 + Au_{10}/POM indicate the slab structure with six water molecules introduced into its defect site, Au_{10} cluster-supported structure, and O_2-adsorbed Au_{10}/POM, respectively. $[SiW_{12}O_{40}]^{4-}$ (1), $[SiW_{12}O_{40}]^{4-}$ (2), and $[SiW_{12}O_{40}]^{4-}$ (3) represent $[SiW_{12}O_{40}]^{4-}$ at the top layer and two $[SiW_{12}O_{40}]^{4-}$ at the bottom layer in the POM slab model shown in Fig. 1(d).

	POM	Au_{10}/POM	O_2 + Au_{10}/POM
$[SiW_{12}O_{40}]^{4-}$ (1)	–3.65	–4.22	–3.82
$[SiW_{12}O_{40}]^{4-}$ (2)	–3.65	–4.06	–4.00
$[SiW_{12}O_{40}]^{4-}$ (3)	–3.68	–3.95	–3.88
Au_{10}	–	+1.29	+1.21
O_2	–	–	–0.47
6 H_2O	–0.07	–0.08	–0.08
12 Cs^+	+11.04	+11.01	+11.03
Sum	0	0	0

charge of +1.29 after its immobilization on $[SiW_{12}O_{40}]^{4-}$. The structure of each atom near the interface and its differential charge are shown in Figure S1 and Table S2, respectively. Electron depletion was particularly localized on the Au atoms near the interface (Au1–Au6). On the other hand, electron accumulation was localized on the O atoms of $[SiW_{12}O_{40}]^{4-}$, particularly O1, O3, O5, O6, and O7, and almost all of them bond with Au_1. As shown in Table 1, the 6 H_2O molecules and 12 Cs^+ cations in the model were unaffected by Au_{10} immobilization and subsequent O_2 adsorption because their charges remained unchanged. This negative charge transfer from Au_{10} to $[SiW_{12}O_{40}]^{4-}$ is in agreement with the DRIFT spectra of adsorbed CO on Au clusters [36], as well as the DFT calculations of $Au_{20}/H_3PW_{12}O_{40}$ conducted by Zhang et al. [66]. CO was activated by adsorption on the positively charged Au atoms at the interface between the Au cluster and the support, which facilitated the CO oxidation reaction. As shown in Figure S1 and Table S2, the Au atoms at the interface of the Au_{10} cluster were positively charged, indicating that they were effective sites for CO adsorption.

3.2. O_2 adsorption

The activation of O_2 is an important process in CO oxidation reactions. Therefore, the adsorption of O_2 on Au_{10}, $[SiW_{12}O_{40}]^{4-}$, and Cs^+ sites in the slab model was investigated. As a result, the adsorption of O_2 on the Au_{10} cluster was the most stable ($E_{ads}(O_2)$ = –0.88 eV). The structures obtained for each O_2 adsorption site are depicted in Figure S2. These results can be explained as follows: Cs^+ cannot strongly anchor O_2, even if Au_{10} is introduced into the slab model, because Cs^+ maintains a closed-shell electronic structure. The W atoms in $[SiW_{12}O_{40}]^{4-}$, which have the potential to adsorb O_2, are sterically hindered by the surrounding O atoms, so O_2 cannot be adsorbed onto W atoms; therefore, Au_{10} is the sole adsorption site in this model.

The differential charges of these components are listed in Table 1. The differential charge of Au_{10} hardly changed after the adsorption of O_2, and adsorbed O_2 is negatively charged, indicating that the electrons have retransferred from $[SiW_{12}O_{40}]^{4-}$ to the adsorbed O_2 via the Au_{10} cluster. To clarify the electronic state of O_2 adsorbed on Au_{10}/POM, the projected density of states (PDOS) of the adsorbed O_2 and Au_{10} were calculated, and the results are shown in Fig. 3. Hybridization between the p band of O_2 and the s and d bands of Au_{10} indicate strong chemisorption of O_2 on Au_{10}. A group of three p bands of adsorbed O_2 (–1.16 eV, –0.72 eV, and –0.56 eV) contributes to the π* orbitals of the O–O bond below the Fermi level (0 eV). This indicates that the adsorbed O_2 is superoxide (O_2^-), resulting from the acceptance of one electron from the surface of the catalyst. As shown in Fig. 4(b), the adsorbed O_2 is a superoxide with three electrons in the π* orbitals. Therefore, it has a unique spin-density shape derived from only one of the π* orbitals, clearly differing from the gas-phase O_2 molecule shown in Fig. 4(a). The elongation of O–O bond from 121 pm to 134 pm is also due to the occupation of the π* antibonding orbital by the electron donated from Au_{10} as well as the negative charge of adsorbed O_2.

3.3. Reaction mechanism of CO oxidation without water molecules

From the results presented in the previous section, the formation of active oxygen species on the Au_{10} surface was confirmed. CO oxidation over Au_{10}/POM without water molecules was investigated to evaluate the reactivity of O_2^- using the slab model shown in Fig. 1(c). As mentioned in the previous section, O_2 may only be adsorbed on the surface of Au_{10} in this model. Also, an experimental study found that CO adsorbs on the positively charged $Au^{\delta+}$ atom [36]. The Eley–Rideal mechanism, in which adsorbed O_2 reacts with CO [67] in the gas phase, is unfavorable for CO oxidation. This is because the activation of O_2 and CO are both important for this reaction [18]. Thus, we examined the Langmuir–Hinshelwood mechanism in which coadsorbed CO and O_2

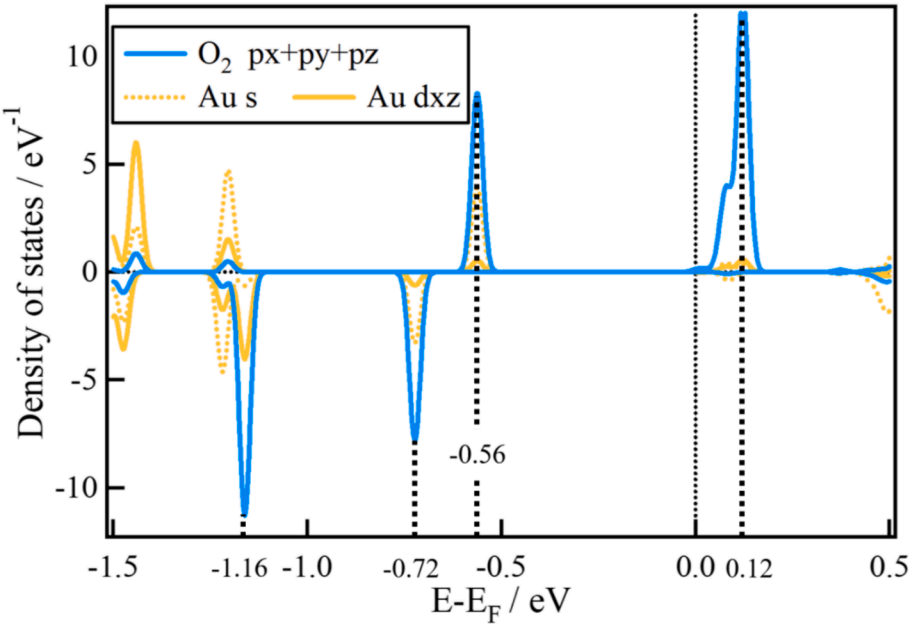

Fig. 3. PDOS of adsorbed O_2 and Au_{10}. E_F is the Fermi energy (eV).

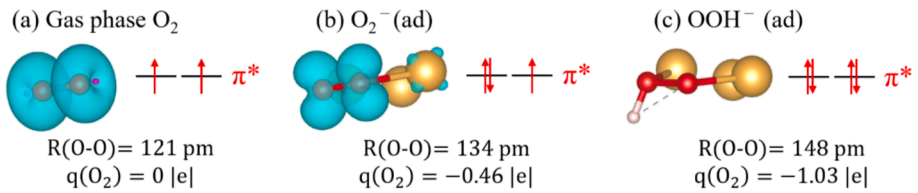

Fig. 4. Spin density, electron configuration of π* orbitals, O–O distance, and differential charges of (a) gas phase (neutral) O_2, (b) adsorbed O_2^- (superoxide), and (c) OOH^- (peroxide). Blue zones represent the spin density. The isosurface of each spin density is set to 0.005 e/\AA. R(O–O) and q(O_2) represent the O–O bond distance and the differential charge of O_2 in each structure, respectively. (For interpretation of the references to colour in this figure legend, the reader is referred to the web version of this article.)

react on the surface of the catalyst [67].

The energy profile and structure of the reaction mechanism are summarized in Fig. 5. Initially, O_2 adsorbs on Au_{10} with an adsorption energy of –0.88 eV and accepts one electron from the catalyst to form a superoxide (IS→IM1). After the adsorption of O_2, CO adsorbs on Au_{10} with an adsorption energy of –1.07 eV (IM1 → IM2). Here, the CO adsorbed on the Au atom in the second layer of Au_{10} was more stable than that adsorbed on the Au atom at the interface, as shown in Figure S3. Even if CO adsorbs on Au_{10} before the adsorption of O_2, the stabilization energy does not change as indicated in Figure S4. Then, the adsorbed CO and O_2 react to form an OCOO surface complex with an activation energy of 0.69 eV. The reaction energy of this process is +0.07 eV (IM2 → TS1 → IM3). By calculating the PDOS and spin density of TS1 (Figure S5), we confirmed that the adsorbed O_2 remained as superoxide during the reaction. Then, the O–O bond of the OCOO surface complex dissociates, and CO_2 desorbs from the Au_{10} surface with an activation energy of 0.23 eV (IM3 → TS2 → IM4). This process is highly exothermic, with a reaction energy of –2.03 eV, owing to the high stability of CO_2. The remaining O adatom on Au_{10} reacts readily with adsorbed CO to form an OCO surface complex, which is then desorbed as CO_2 (IM4 → TS3 → IM6 → TS4 → FS). These processes are moderate and exothermic, with almost negligible activation barriers owing to the very weak interaction between the O adatom and Au_{10}. The reaction step that the adsorbed CO and O_2 react to form the OCOO surface complex (IM2 → TS1 → IM3) has the largest activation energy of 0.69 eV, which is too high a barrier for the process to proceed at temperatures below 0 °C, where Au/POM exhibits high CO oxidation activity [36].

In the experimental study, Au cluster that has a diameter of 2.0 nm had the highest catalytic activity compared to those have diameters of 4.2 nm and 10.7 nm. However, Au_{10} in our slab model has a smaller diameter of 0.6 nm. To examine how the difference of the size of Au cluster affect to the catalytic reaction, we calculated the deformation energies of Au_{10} in each reaction step. The results are summarized in Table S3. Each deformation energy was calculated using the Au_{10}/POM structure with all adsorbates removed from each state. Each structure was not relaxed at this time. From the relative and deformation energies of IM1 and IM2, the adsorption energies of oxygen and CO molecules seem to be slightly larger than the adsorption energies on the large clusters. TS3 has the largest deformation energy of 1.12 eV among them. There are only ten Au atoms in our model, so the deformation energies are thought to be larger than those in real Au nanoclusters with a diameter of 2 nm. It is also known that the junction structure between the nanoclusters and the support and the junction area per unit volume play an important role in Au nanocluster-supported catalysts [3]. In this regard, our model is considered to be a reasonable model for catalytic activity because the junction area per unit volume of clusters is also

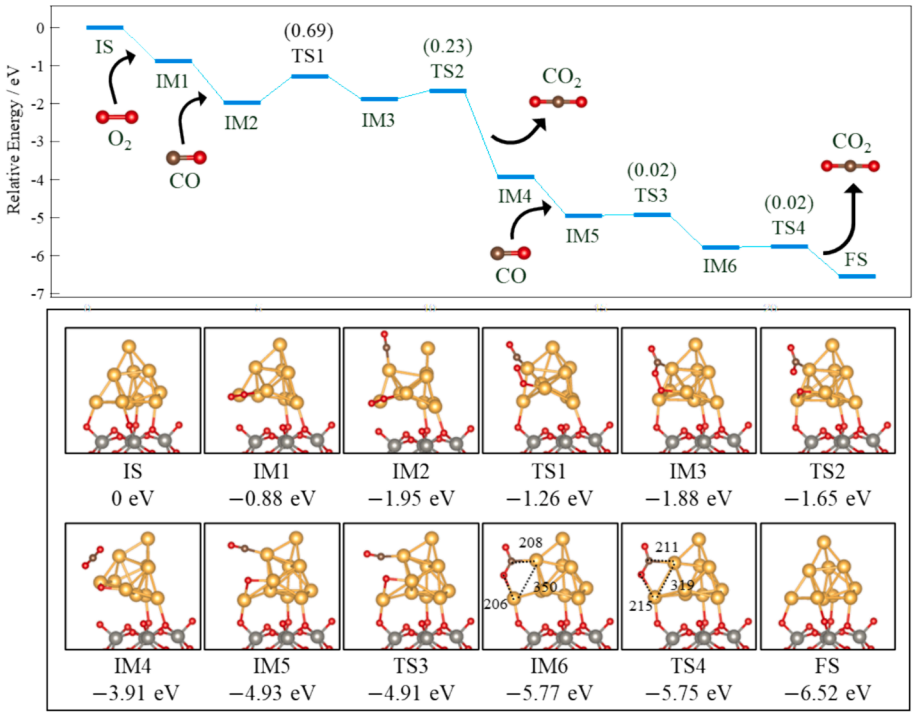

Fig. 5. Energy profile and each structure obtained along the reaction pathway of CO oxidation over $Au_{10}/Cs_4[SiW_{12}O_{40}]$ in the absence of water molecules. The activation energies (eV) of each process are shown in parentheses in the energy diagram. Each value of the energy indicates the relative energy (ΔE) when that of IS is set to 0 eV. The bond distances of C–Au, O–Au, and Au–Au (pm) are shown in the structures of IM6 and TS4.

considered to be large. Considering these results, the adsorption of substrate onto the clusters is somewhat larger, but it seems to be roughly offset by destabilization due to deformation of the clusters. Therefore, although the activation barriers and adsorption energies change depending on the deformability of the clusters, they are not expected to dramatically change the qualitative reaction mechanism. Thus, our small Au_{10} is also thought to have catalytic reaction mechanisms identical to those of larger Au nanoclusters.

3.4. Role of moisture and reaction mechanism for CO oxidation with water molecules

Because the activation barrier of the step of OCOO surface complex formation was significant, CO oxidation over Au_{10}/POM without the influence of water molecules was not catalytically active at low temperatures. Therefore, the reaction mechanism of H_2O-mediated CO oxidation over the Au_{10}/POM model was investigated, as shown in Fig. 1 (d). Saavedra et al. reported that O_2 adsorbed on Au clusters supported on hydroxylated rutile-TiO_2 accepts a proton from Ti–OH to form Au–OOH, which promotes CO oxidation [15]. In this process, water molecules are adsorbed on the surface of the reducible support; therefore, deprotonated species such as Ti–OH and Ti–O can be stabilized by electron donation from the reducible surface. By contrast, because POM is an oxidative material, the deprotonated hydroxyl anion species cannot be stabilized on the catalyst surface, making protonation of the adsorbed O_2 difficult. Accordingly, the deprotonated species are thought to be stabilized by water molecules themselves. As mentioned in the previous section, $Cs_4[SiW_{12}O_{40}]$ has one $[SiW_{12}O_{40}]^{4-}$ defect site out of four to compensate for the excess negative charge of $[SiW_{12}O_{40}]^{4-}$ and holds water molecules in the defect site. The spatial distance between the defect site and the adjacent $[SiW_{12}O_{40}]^{4-}$ site across the Cs^+ site makes it difficult for the water molecules in the defect site to donate a proton directly to the O_2 adsorbed on Au_{10}. Therefore, we connected Au_{10} and the water molecules at the defect sites with three bridging water molecules. Here, the adsorption of three bridging water molecules is highly exothermic, with an adsorption energy of –0.67 eV per water molecule. It was calculated that O_2 adsorbed on Au_{10} indirectly accepted a proton from water molecules and formed OOH species, as shown in Fig. 6. This process has an activation energy of 0.31 eV and a reaction energy of +0.02 eV (IM1′→TS1′→IM2′). As mentioned previously, the number of water molecules in the slab model is the minimum required to maintain the crystalline structure of $Cs_4[SiW_{12}O_{40}]$. In real systems, more water molecules are assumed to be present on the catalyst surface. Therefore, this reaction pathway is considered reasonable, as it is expected to stabilize the remaining OH^- species in the water molecules.

To clarify the electronic structure of the OOH species formed on Au_{10}, the PDOS of O and Au were calculated. The results are presented in Fig. 7. Four bands of oxygen p orbitals appear at –0.30 eV and –0.09 eV, which are attributed to the π* orbitals of the O–O bond. This indicates that peroxide (OOH^-) is formed on Au_{10}, which has accepted two electrons from the surface of Au_{10}/POM. Fig. 4(c) shows that the O–O bond elongates from 134 pm in the superoxide to 148 pm in the peroxide, and the negative charge of O_2 increases. Also, no spin density occurs on the OOH species because the π* orbital of the O–O bond is completely occupied.

The CO oxidation mechanism following OOH^- formation was also calculated. The energy diagrams and structures of this mechanism are shown in Fig. 8. The initial state (IS') of this reaction is free of O_2 and CO but contains three cross-linked water molecules on its surface. First, O_2 is adsorbed on Au_{10} with an adsorption energy of –0.97 eV (IS'→IM1′). This adsorption energy is a little larger than that of the model without cross-linked water molecules (–0.88 eV) owing to the hydrogen bond between the adsorbed O_2 and one of the three cross-linked water molecules. As explained before, the adsorbed O_2^- accepts a proton from water molecules in the defect site to form OOH^-, with an activation energy of 0.31 eV and a reaction energy of +0.02 eV (IM1′→TS1′→IM2′). Additionally, the decomposition of OOH^- is unfavorable because there is a high activation barrier of 1.10 eV and a destabilization energy of +0.53 eV as shown in Figure S6. Next, CO adsorbs on Au_{10} (IM2′→IM3′) with an adsorption energy of –1.00 eV. The CO adsorbed on the Au atom at the interface is more stable than that adsorbed on the Au atom in the second layer, as shown in Figure S3. Then, the OOH^- transfers from the side on form to the endon form with an activation energy of 0.05 eV and reaction energy of +0.02 eV. (IM3′→TS2′→IM4′) This step is not crucial, but it prevents steric hindrance between adsorbed CO and the OOH^- species. In this step, there is no change in the electronic structure of the

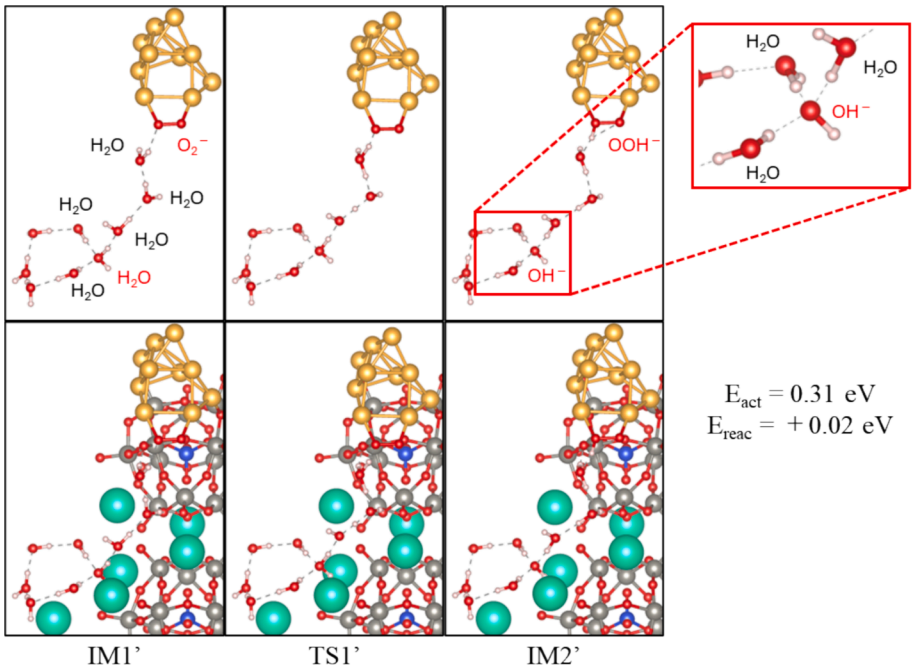

Fig. 6. Formation of OOH species on Au_{10} in the presence of water molecules in the defect site. E_{act} and E_{reac} are the activation energy and reaction energy of this process, respectively.

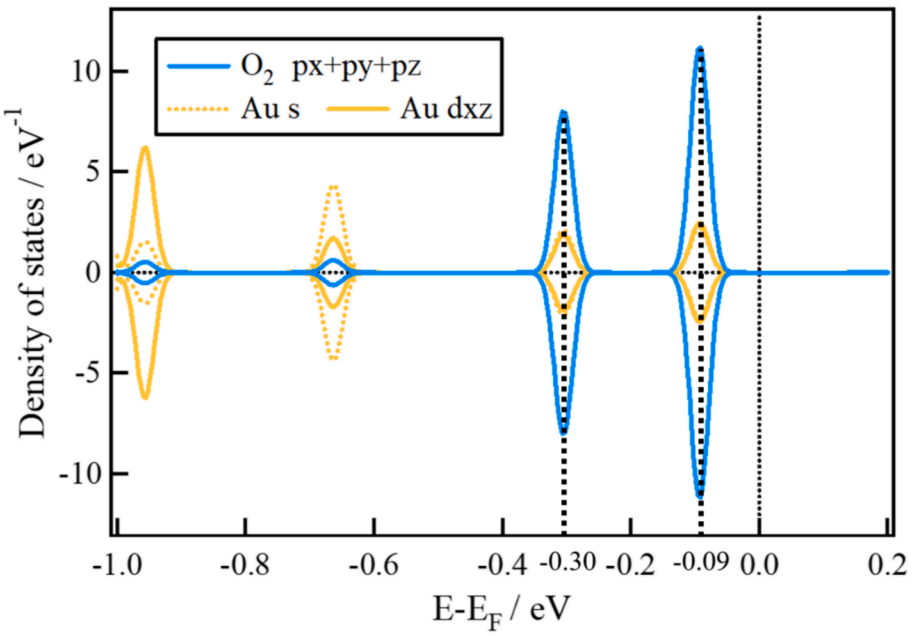

Fig. 7. Projected density of states (PDOS) of O_2 of OOH species and Au_{10}. E_F is the Fermi energy (eV).

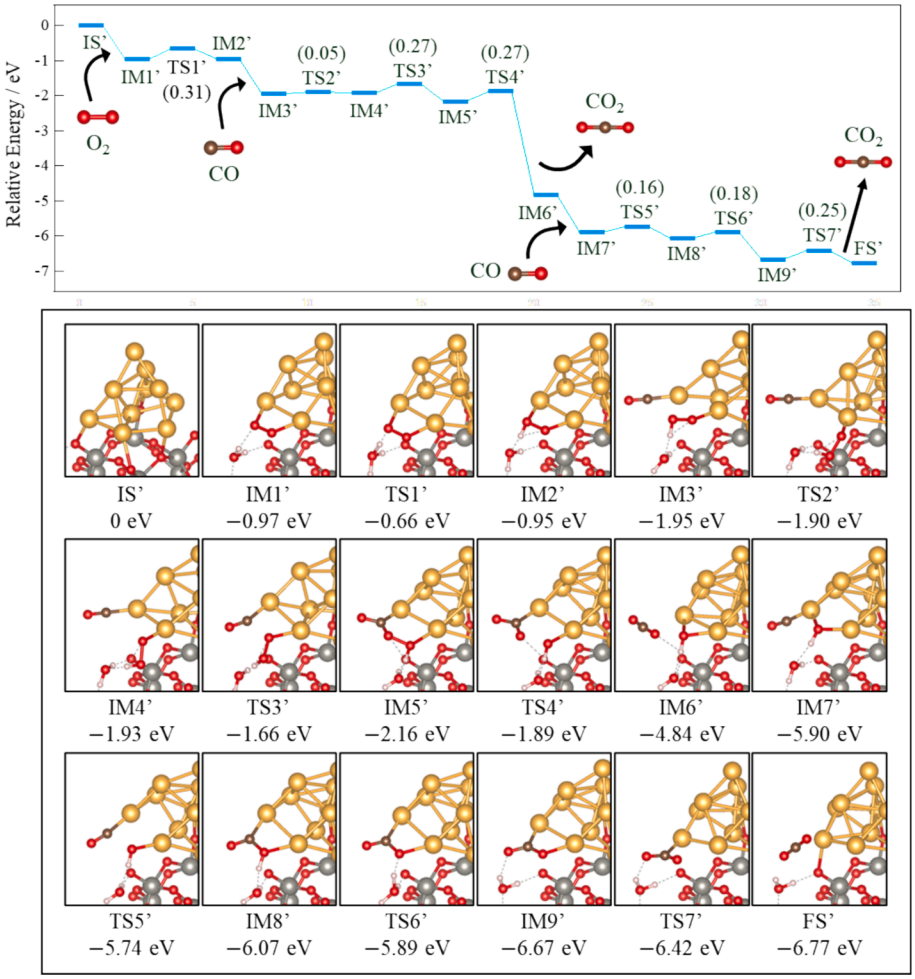

Fig. 8. Energy profile and each structure obtained along the reaction pathway of CO oxidation over $Au_{10}/Cs_4[SiW_{12}O_{40}]$ in the presence of water molecules in the defect site. The activation energies (eV) of each process are shown in parentheses in the energy diagram. Each value of the energy indicates the relative energy (ΔE) when that of IS' is set to 0 eV.

OOH species, as shown in Figure S7. The adsorbed CO and the endon OOH^- react to form the OCOOH surface complex on Au_{10} (IM4′→TS3′→IM5′). The activation energy of this process is 0.27 eV, and this process is exothermic, with a reaction energy of –0.23 eV. The cleavage of the O–O bonding moiety decomposes the OCOOH, and CO_2 is desorbed from the surface, with an activation energy of 0.27 eV and a reaction energy of –2.68 eV (IM5′→TS4′→IM6′). This process exhibited a strong exotherm owing to the high stability of CO_2 desorbed from the surface of Au_{10}/POM. The OH species remaining on the surface react with adsorbed CO, with an activation energy of 0.16 eV and a reaction energy of –0.17 eV, to form a COOH surface complex (IM6′→IM7′→TS5′→IM8′). It was confirmed that the OH species cannot dissociate and return a proton to the remaining OH^- species in the pore, as shown in Figure S8. Finally, COOH decomposes into CO_2 in two steps (IM8′→TS6′→IM9′→TS7′→FS'). After the COOH surface complex returns a proton to the OH^- species in the defect site, CO_2 desorbs from the catalyst surface. These two steps are downhill, and their activation energies are 0.18 eV and 0.25 eV, respectively. In FS', no adsorbates existed, as in IS,' and the catalytic cycle was complete.

The first reaction step that adsorbed O_2^- accepts a proton from water molecules to form OOH^- (IM1′→TS1′→IM2′) has the largest activation energy of 0.31 eV in this reaction pathway. This activation energy is sufficiently low for the process to proceed even at temperatures below 0 °C. In addition, the activation energy of the reaction between OOH^- and CO (0.27 eV, IM4′→TS3′→IM5′) is much lower than that of the reaction between O_2^- and CO (0.69 eV, IM2 → TS1 → IM3) because OOH^- (peroxide) is more activated than O_2^- (superoxide), thus facilitating CO oxidation.

In order to examine the temperature dependency of the adsorption strength of water molecules, we calculated the Gibbs free energies for the adsorption of water molecules at each temperature from ⁻80 °C to 240 °C where the catalytic experiments were conducted in the previous study [36]. The results are shown in Figure S9, which indicates that the adsorption of water molecules is energetically unfavorable above 47 °C. This result is qualitatively consistent with the experimental results, in which catalytic activity decreases above 60 °C. Thus, CO oxidation reactions involving water molecules adsorbed on the surface of the catalyst proceed readily at low temperatures, with relatively low activation barriers. However, at higher temperatures, the surface-adsorbed water molecules desorb, and the reaction mechanism no longer involves the water molecules in the defect site. Because the activation barriers in the absence of water molecules are significantly higher than those for reactions involving surface-adsorbed water, the catalytic activity is expected to decrease. Therefore, we conclude that this switch in the reaction mechanism is responsible for the experimentally obtained, inverted U-shaped CO conversion curve.

4. Conclusion

Using DFT calculations, we investigated the catalytic reaction mechanism of CO oxidation over Au_{10}/POM with and without water molecules. In general, the supports of Au cluster catalysts that exhibit high CO oxidation activity are reducible metal oxides, whereas POM is an acidic support that does not exhibit high CO oxidation activity. However, it was experimentally demonstrated that Au/POM catalysts exhibit high CO oxidation activity in the presence of water molecules below room temperature. Our calculations revealed that water molecules adsorbed in the defect site interact with O_2 adsorbed on the surface of the Au cluster to form the OOH^- species, which is highly active for CO oxidation. Even in the absence of water molecules, O_2^- species can be generated on the Au cluster, but their CO oxidation activity is lower than that of OOH^- species. From these results, we qualitatively determined that in the low-temperature region where the catalyst has a high activity, the reaction proceeds via a mechanism involving water. By contrast, in the high-temperature region where the activity is lower, the reaction proceeds via a mechanism that does not involve water molecules owing to the desorption of water molecules from the catalyst surface. This results in an inverted U-shaped CO conversion curve, as observed in a previous study [36]. The fact that CO oxidation activity increases simply by introducing water molecules on the surface, without changing the substrate state, informs future catalyst research.

Funding sources

Any funds used to support the research of the manuscript should be placed here (per journal style).

CRediT authorship contribution statement

Tomohisa Yonemori: Writing – original draft, Data curation. **Yasutaka Hamada:** Formal analysis, Data curation. **Tamao Ishida:** Writing – review & editing, Validation, Investigation. **Toru Murayama:** Writing – review & editing, Investigation, Formal analysis. **Takashi Kawakami:** Writing – review & editing, Validation. **Shusuke Yamanaka:** Writing – review & editing, Validation, Investigation. **Mitsutaka Okumura:** Writing – review & editing, Validation, Project administration, Investigation, Funding acquisition, Conceptualization.

Declaration of competing interest

The authors declare that they have no known competing financial interests or personal relationships that could have appeared to influence the work reported in this paper.

Data availability

No data was used for the research described in the article.

Acknowledgment

M. O. received funding from JSPS KAKENHI, Japan 22H00274and 21K04994 and T. M. from 22H00282, 23K26456. This work was partially supported by the Joint Usage/Research Center for Catalysis.

Appendix A. Supplementary material

Supplementary material to this article can be found online at https://doi.org/10.1016/j.jcat.2024.115724.

References

[1] M. Haruta, T. Kobayashi, H. Sano, N. Yamada, Novel gold catalysts for the oxidation of carbon monoxide at a temperature far below 0 ℃, Chem. Lett. 16 (1987) 405–408, https://doi.org/10.1246/cl.1987.405.
[2] M. Haruta, N. Yamada, T. Kobayashi, S. Iijima, Gold catalysts prepared by coprecipitation for low-temperature oxidation of hydrogen of carbon-monoxide, J. Catal. 115 (1989) 301–309, https://doi.org/10.1016/0021-9517(89)90034-1.
[3] T. Takei, T. Akita, I. Nakamura, T. Fujitani, M. Okumura, K. Okazaki, J.H. Huang, T. Ishida, M. Haruta, Heterogeneous catalysis by gold, Adv. Catal. 55 (2012) 1–126, https://doi.org/10.1016/B978-0-12-385516-9.00001-6.
[4] Q. Fu, H. Saltsburg, S.M. Flytzani, Active nonmetallic Au and Pt species on ceria-based water-gas shift catalysts, Science 301 (2003) 935–938, https://doi.org/10.1126/science.1085721.
[5] L.C. Wang, D. Widmann, R.J. Behm, Reactive removal of surface oxygen by H_2, CO and CO/H_2 on a Au/CeO_2 catalyst and its relevance to the preferential CO oxidation (PROX) and reverse water gas shift (RWGS) reaction, Catal. Sci. Technol. 5 (2015) 925–941, https://doi.org/10.1039/C4CY01030B.
[6] T. Hayashi, K. Tanaka, M. Haruta, Selective vapor-phase epoxidation of propylene over Au/TiO_2 catalysts in the presence of oxygen and hydrogen, J. Catal. 178 (1998) 566–575, https://doi.org/10.1006/jcat.1998.2157.
[7] M. Haruta, B.S. Uphade, S. Tsubota, A. Miyamoto, Selective oxidation of propylene over gold deposited on titanium-based oxides, Res. Chem. Intermed. 24 (1998) 329–336, https://doi.org/10.1163/156856798X00276.
[8] I. Kamiya, H. Tsunoyama, T. Tsukuda, H. Sakurai, Lewis acid character of zero-valent gold nanoclusters under aerobic conditions: Intramolecular hydroalkoxylation of alkenes, Chem. Lett. 36 (2007) 646–647, https://doi.org/10.1246/cl.2007.646.

[9] T. Ishida, T. Murayama, A. Taketoshi, M. Haruta, Importance of size and contact structure of gold nanoparticles for the genesis of unique catalytic processes, Chem. Rev. 120 (2019) 464–525, https://doi.org/10.1021/acs.chemrev.9b00551.
[10] M. Okumura, M. Haruta, Interplay of Theoretical calculations and experiments for a study of catalysis by gold, Catal. Today 259 (2016) 81–86, https://doi.org/10.1016/j.cattod.2015.05.006.
[11] H. Koga, K. Tada, M. Okumura, Density functional theory study of active oxygen at the perimeter of Au/TiO_2 catalysts, J. Phys. Chem. C 119 (2015) 25907–25916, https://doi.org/10.1021/acs.jpcc.5b07633.
[12] M. Daté, M. Okumura, S. Tsubota, M. Haruta, Vital role of moisture in the catalytic activity of supported gold nanoparticles, Angew. Chem., Int. Ed. 43 (116) (2004) 2181–2184, https://doi.org/10.1002/anie.200453796.
[13] D. Widmann, R.J. Behm, Activation of molecular oxygen and the nature of the active oxygen species for CO oxidation on oxide supported Au catalysts, Acc. Chem. Res. 47 (2014) 740–749, https://doi.org/10.1021/ar400203e.
[14] M. Daté, M. Haruta, Moisture effect on CO oxidation over Au/TiO_2 catalyst, J. Catal. 201 (2001) 221–224, https://doi.org/10.1006/jcat.2001.3254.
[15] J. Saavedra, H.A. Doan, C.J. Pursell, L.C. Grabow, B.D. Chandler, The critical role of water at the gold-titania interface in catalytic CO oxidation, Science 345 (2014) 1599–1602, https://doi.org/10.1126/science.1256018.
[16] J. Saavedra, C.J. Pursell, B.D. Chandler, CO oxidation kinetics over Au/TiO_2 and Au/Al_2O_3 catalysts: evidence for a common water-assisted mechanism, J. Am. Chem. Soc. 140 (140) (2018) 3712–3723, https://doi.org/10.1021/jacs.7b12758.
[17] H. Koga, K. Tada, M. Okumura, DFT study of CO oxidation catalyzed by Au/TiO_2: activity of small clusters, e-J Surf. Sci. Nanotechnol. 13 (2015) 129–134, https://doi.org/10.1380/ejssnt.2015.129.
[18] H. Koga, K. Tada, M. Okumura, DFT study of CO oxidation over Au/TiO_2 (110): the extent of the reactive perimeter zone, Chem. Phys. Lett. 610 (2014) 76–81, https://doi.org/10.1016/j.cplett.2014.06.061.
[19] I.X. Green, W. Tang, M. Neurock, J.T.J. Yates, Spectroscopic observation of dual catalytic sites during oxidation of CO on a Au/ TiO_2 catalyst, Science 333 (2011) 736–739, https://doi.org/10.1126/science.1207272.
[20] I.X. Green, W.J. Tang, M. McEntee, M. Neurock, J.T. Yates, Inhibition at perimeter sites of Au/TiO_2 oxidation catalyst by reactant oxygen, J. Am. Chem. Soc. 134 (2012) 12717–12723, https://doi.org/10.1021/ja304426b.
[21] L.M. Molina, M.D. Rasmussen, B. Hammer, Adsorption of O_2 and oxidation of CO on Au nanoparticles supported by TiO_2 (110), J. Chem. Phys. 120 (2004) 7673–7680, https://doi.org/10.1063/1.1687337.
[22] P. Schlexer, D. Widmann, R.J. Behm, G. Pacchioni, CO oxidation on a Au/TiO_2 nanoparticle catalyst via the Au-assisted Mars–van Krevelen mechanism, ACS Catal. 8 (2018) 6513–6525, https://doi.org/10.1021/acscatal.8b01751.
[23] T. Fujita, T. Ishida, K. Shibamoto, T. Honma, H. Ohashi, T. Murayama, M. Haruta, CO oxidation over Au/ZnO: unprecedented change of the reaction mechanism at low temperature caused by a different O_2 activation process, ACS Catal. 9 (2019) 8364–8372, https://doi.org/10.1021/acscatal.9b02128.
[24] M. Lin, C. Mochizuki, Y. Inomata, T. Ishida, M. Haruta, T. Murayama, Elucidation of active sites of gold nanoparticles on acidic Ta_2O_5 supports for CO oxidation, ACS Catal. 10 (2020) 9328–9335, https://doi.org/10.1021/acscatal.0c01966.
[25] D. Widmann, R.J. Behm, Active oxygen on a Au/TiO_2 catalyst: formation, stability, and CO oxidation activity, Angew. Chem., Int. Ed. 43 (2011) 10241–10245, https://doi.org/10.1002/anie.201102062.
[26] D.A.H. Cunningham, W. Vogel, M. Haruta, Negative activation energies in CO oxidation over an icosahedral Au/$Mg(OH)_2$ catalyst, Catal. Lett. 63 (1999) 43–47, https://doi.org/10.1023/A:1019088131252.
[27] Y. Wang, D. Widmann, F. Lehnert, D. Gu, F. Schüth, R.J. Behm, Avoiding self-poisoning: a key feature for the high activity of Au/$Mg(OH)_2$ catalysts in continuous low-temperature CO oxidation, Angew. Chem., Int. Ed. 56 (2017) 9597–9602, https://doi.org/10.1002/anie.201702178.
[28] W. Vogel, D.A.H. Cunningham, K. Tanaka, M. Haruta, Structural Analysis of Au/$Mg(OH)_2$ during Deactivation by Debye Function Analysis, Catal. Lett. 40 (1996) 175–181, https://doi.org/10.1007/BF00815279.
[29] D.A.H. Cunningham, W. Vogel, H. Kageyama, S. Tsubota, M. Haruta, The relationship between the structure and activity of nanometer size gold when supported on $Mg(OH)_2$, J. Catal. 177 (1998) 1–10, https://doi.org/10.1006/jcat.1998.2050.
[30] M. Haruta, K. Saika, T. Kobayashi, S. Tsubota, Y. Nakahara, Preparation and catalytic properties of gold finely dispersed on beryllium oxide, Chem. Express 3 (1988) 159–162, https://doi.org/10.1002/chin.198820029.
[31] H. Lian, M. Jia, W. Pan, Y. Li, W. Zhang, D. Jiang, Gold-base catalysts supported on carbonate for low-temperature CO oxidation, Catal. Commun. 6 (2005) 47–51, https://doi.org/10.1016/j.catcom.2004.10.012.
[32] N. Phonthammachai, Z. Ziyi, G. Jun, H.Y. Fan, T.J. White, Synthesis of high performance hydroxyapatite-gold catalysts for CO oxidation, Gold Bull. 41 (2008) 42–50, https://doi.org/10.1007/BF03215622.
[33] S. Omwoma, C.T. Gore, Y. Ji, C. Hu, Y.F. Song, Environmentally benign polyoxometalate materials, Coord. Chem. Rev. 286 (2015) 17–29, https://doi.org/10.1016/j.ccr.2014.11.013.
[34] K. Piepgrass, M.T. Pope, Oxygen atom transfer chemistry of heteropolytungstate 'browns' in nonaqueous solvents, J. Am. Chem. Soc. 111 (1989) 753–754, https://doi.org/10.1021/ja00184a065.
[35] I.A. Weinstock, E.M. Barbuzzi, M.W. Wemple, J.J. Cowan, R.S. Reiner, D. M. Sonnen, R.A. Heintz, J.S. Bond, C.L. Hill, Equilibrating metal-oxide cluster ensembles for oxidation reactions using oxygen in water, Nature 414 (2001) 191–195, https://doi.org/10.1038/35102545.
[36] T. Yoshida, T. Murayama, N. Sakaguchi, M. Okumura, T. Ishida, M. Haruta, Carbon monoxide oxidation by polyoxometalate-supported gold nanoparticulate catalysts: activity, stability, and temperature-dependent activation properties, Angew. Chem., Int. Ed. 130 (2018) 1539–1543, https://doi.org/10.1002/ange.201710424.
[37] G. Kresse, J. Furthmuller, Efficiency of ab-initio total energy calculations for metals and semiconductors using a plane-wave basis set, Comput. Mater. Sci. 6 (1996) 15–50, https://doi.org/10.1016/0927-0256(96)00008-0.
[38] G. Kresse, J. Furthmuller, Efficient iterative schemes for ab initio total-energy calculations using a plane-wave basis set, Phys. Rev. B 54 (1996) 11169–11186, https://doi.org/10.1103/PhysRevB.54.11169.
[39] J. Perdew, K. Burke, M. Ernzerhof, Generalized gradient approximation made simple, Phys. Rev. Lett. 77 (1996) 3865–3868, https://doi.org/10.1103/PhysRevLett.77.3865.
[40] G. Kresse, D. Joubert, From ultrasoft pseudopotentials to the projector augmented-wave method, Phys. Rev. B: Condens. Matter Mater. Phys. (1999) 1758–1775, https://doi.org/10.1103/PhysRevB.59.1758.
[41] P. Blochl, Projector augmented-wave method, Phys. Rev. B 50 (1994) 17953–17979, https://doi.org/10.1103/PhysRevB.50.17953.
[42] R. Bader, in: Atoms in Molecules: a Quantum Theory, Oxford University Press, New York, 1990, https://doi.org/10.1093/oso/9780198551683.001.0001.
[43] H.J. Monkhorst, J.D. Pack, Special Points for Brillouin-zone Integrations, Phys. Rev. B: Condens. Matter Mater. Phys. 13 (1976) 5188–5192, https://doi.org/10.1103/PhysRevB.13.5188.
[44] C.M. Capdevila, Z. Łodziana, N. López, Performance of DFT+U approaches in the study of catalytic materials, ACS Catal. 6 (2016) 8370–8379, https://doi.org/10.1021/acscatal.6b01907.
[45] S. Grimme, J. Antony, S. Ehrlich, H.A. Krieg, Consistent and accurate ab initio parametrization of density functional dispersion correction (DFT-D) for the 94 Elements H−Pu, J. Chem. Phys. 132 (2010) 154104, https://doi.org/10.1063/1.3382344.
[46] W.H. Press, B.P. Flannery, S.A. Teukolsky, W.T. Vetterling, in: Numerical Recipes, 2nd ed., Cambridge University Press, New York, 1990 https://doi.org/10.1007/BF01321860.
[47] M. Hestenes, E. Stiefel, Methods of conjugate gradients for solving linear systems, J. Res. Natl. Bur. Stand. 49 (1952) 409–436. https://api.semanticscholar.org/CorpusID:2207234.
[48] J. Nocedal, Updating quasi-Newton matrices with limited storage, Math. Comput. 35 (1980) 773–782, https://doi.org/10.1090/S0025-5718-1980-0572855-7.
[49] D. Shanno, Conditioning of quasi-Newton methods for function minimization, Math. Comput. 24 (1970) 647–656, https://doi.org/10.1090/S0025-5718-1970-0274029-X.
[50] G. Henkelman, H. Jonsson, Improved tangent estimate in the nudged elastic band method for finding minimum energy paths and saddle points, J. Chem. Phys. 113 (2000) 9978–9985, https://doi.org/10.1063/1.1323224.
[51] D. Sheppard, G. Henkelman, Paths to which the nudged elastic band converges, J. Comput. Chem. 32 (2011) 1769–1771, https://doi.org/10.1002/jcc.21748.
[52] D. Sheppard, P. Xiao, W. Chemelewski, D.D. Johnson, G.A. Henkelman, generalized solid-state nudged elastic band method, J. Chem. Phys. 136 (2012) 074103, https://doi.org/10.1063/1.3684549.
[53] D. Sheppard, R. Terrell, G. Henkelman, Optimization methods for finding minimum energy paths, J. Chem. Phys. 128 (2008) 134106, https://doi.org/10.1063/1.2841941.
[54] G. Henkelman, B. Uberuaga, H. Jonsson, A climbing image nudged elastic band method for finding saddle points and minimum energy paths, J. Chem. Phys. 113 (2000) 9901–9904, https://doi.org/10.1063/1.1329672.
[55] G. Henkelman, H. Jonsson, A dimer method for finding saddle points on high dimensional potential surfaces using only first derivatives, J. Chem. Phys. 111 (1999) 7010–7022, https://doi.org/10.1063/1.480097.
[56] A. Heyden, A. Bell, F. Keil, Efficient methods for finding transition states in chemical reactions: Comparison of improved dimer method and partitioned rational function optimization method, J. Chem. Phys. 123 (2005) 224101, https://doi.org/10.1063/1.2104507.
[57] J. Kaestner, P. Sherwood, Superlinearly converging dimer method for transition state search, J. Chem. Phys. 128 (2008) 014106, https://doi.org/10.1063/1.2815812.
[58] P. Xiao, D. Sheppard, J. Rogal, G. Henkelman, Solid-state dimer method for calculating solid-solid phase transitions, J. Chem. Phys. 140 (2014) 174104, https://doi.org/10.1063/1.4873437.
[59] A.H. Larsen, J.J. Mortensen, J. Blomqvist, I.E. Castelli, R. Christensen, M. Dulak, J. Friis, M.N. Groves, B. Hammer, C. Hargus, E.D. Hermes, P.C. Jennings, P. B. Jensen, J. Kermode, J.R. Kitchin, E.L. Kolsbjerg, J. Kubal, K. Kaasbjerg, S. Lysgaard, J.B. Maronsson, T. Maxson, T. Olsen, L. Pastewka, A. Peterson, C. Rostgaard, J. Schiøtz, O. Schütt, M. Strange, K.S. Thygesen, T. Vegge, L. Vilhelmsen, M. Walter, Z. Zeng, K.W. Jacobsen, The atomic simulation environment—a python library for working with atoms, J. Phys.: Condens. Matter. 29 (2017) 273002, https://doi.org/10.1088/1361-648X/aa680e.
[60] K. Momma, F. Izumi, VESTA 3 for three-dimensional visualization of crystal, volumetric and morphology data, J. Appl. Crystallogr. 44 (2011) 1272–1276, https://doi.org/10.1107/S0021889811038970.
[61] J.F. Keggin, Structure of the molecule of 12-phosphotungstic acid, Nature 131 (1933) 908–909, https://doi.org/10.1038/131908b0.
[62] X. Lopez, J.M. Maestre, C. Bo, J.M. Poblet, Electronic properties of polyoxometalates: A DFT study of α/β-[XM12O40] n-relative stability (M= W, Mo and X a main group element), J. Am. Chem. Soc. 123 (2001) 9571–9576, https://doi.org/10.1021/ja010768z.
[63] C.G. Liu, M.X. Jiang, Z.M. Su, Computational study on M_1/POM single-atom catalysts (M= Cu, Zn, Ag, and Au; POM=$[PW_{12}O_{40}]^{3-}$): metal–support interactions

and catalytic cycle for alkene epoxidation, Inorg. Chem. 56 (2017) 10496–10504, https://doi.org/10.1021/acs.inorgchem.7b01480.

[64] N. Hiyoshi, Y. Kamiya, Observation of microporous cesium salts of 12-tungstosilicic acid using scanning transmission electron microscopy, Chem. Commun. 51 (2015) 9975–9978, https://doi.org/10.1039/C5CC01842K.

[65] Y. Ogasawara, S. Uchida, T. Maruichi, R. Ishikawa, N. Shibata, Y. Ikuhara, N. Mizuno, Cubic cesium hydrogen silicododecatungstate with anisotropic morphology and polyoxometalate vacancies exhibiting selective water sorption and cation-exchange properties, Chem. Mater. 25 (2013) 905–911, https://doi.org/10.1021/cm3039448.

[66] J. Zhang, X. Liu, M.N. Hedhili, Y. Zhu, Y. Han, Highly selective and complete conversion of cellobiose to gluconic acid over Au/$Cs_2HPW_{12}O_{40}$ nanocomposite catalyst, Chem. Cat. Chem. 3 (2011) 1294–1298, https://doi.org/10.1002/cctc.201100106.

[67] R.J. Baxter, P. Hu, Insight into why the Langmuir-Hinshelwood mechanism is generally preferred, J. Chem. Phys. 116 (2002) 4379–4381, https://doi.org/10.1063/1.1458938.